Li *et al. Biochar* (2026) 8:117
https://doi.org/10.1007/s42773-026-00625-9

Biochar

ORIGINAL RESEARCH Open Access

Synergetic polyethylene microplastic photodegradation over core–shell TiO_2/biochar: unraveling the dual roles of interfacial bonding and biochar-derived DOM

Zuolong Li[1], Shihan Chen[1], Yue Sun[1], Yang Ding[2], Cheng Chen[1] and Jiehong He[1*]

Abstract

The pervasive accumulation of polyethylene (PE) microplastics (MPs) from agricultural mulch films represents a critical threat to soil health and ecological stability. In this study, we developed a sustainable "waste-to-resource" strategy by engineering biomass-derived biochar/core–shell TiO_2 (BC/CST) composites for the efficient remediation of PE-MPs. Walnut shell biochar-optimized core–shell structural TiO_2 composites (12TJBC) achieved superior performance, reducing PE-MPs size from 500 μm to <70 μm within 40 h, outpacing pristine TiO_2 by 2.8-fold. Systematic characterization revealed that the superior activity originates from the synergistic effects of Ti–O–C interfacial bonding and bandgap narrowing (from 3.19 to 2.74 eV), which facilitates efficient charge separation and visible-light harvesting. Mechanistic investigations identified hydroxyl radicals (•OH) as the dominant reactive oxygen species (ROS), with steady-state concentrations reaching 8.84 μM. A unique focus was placed on the environmental chemistry of biochar-derived dissolved organic matter (JDOM). We found that JDOM acts as a co-catalyst to amplify degradation by enhancing electron-accepting capacity, effectively counteracting its inherent light-shielding effects. Furthermore, the chemical fate of PE-MPs was elucidated through two-dimensional correlation spectroscopy (2D-COS) and GC–MS, revealing a sequential oxidation pathway from long-chain alkanes to low-toxicity oxygenated intermediates. Ecotoxicological assessments via ECOSAR confirmed the environmental safety of the products. This work provides a dual-phase synergistic framework for mitigating plastic pollution while ensuring ecotoxicological integrity in agricultural ecosystems.

Highlights

- Various core–shell TiO_2/biochar composites were successfully prepared.
- Walnut shell biochar enhanced interfacial charge transfer via Ti–O-C bonds.
- Hydroxyl radicals dominated the photocatalytic PE microplastics degradation.
- Biochar-derived DOM amplified ROS generation without light-shielding effects.
- A stepwise degradation pathway of PE microplastics was resolved via 2D-COS and GC–MS.

Keywords Polyethylene microplastics, Photocatalysis, Biochar, TiO_2, DOM

*Correspondence:
Jiehong He
jiehonghe@ahau.edu.cn
Full list of author information is available at the end of the article

Springer

Graphical Abstract

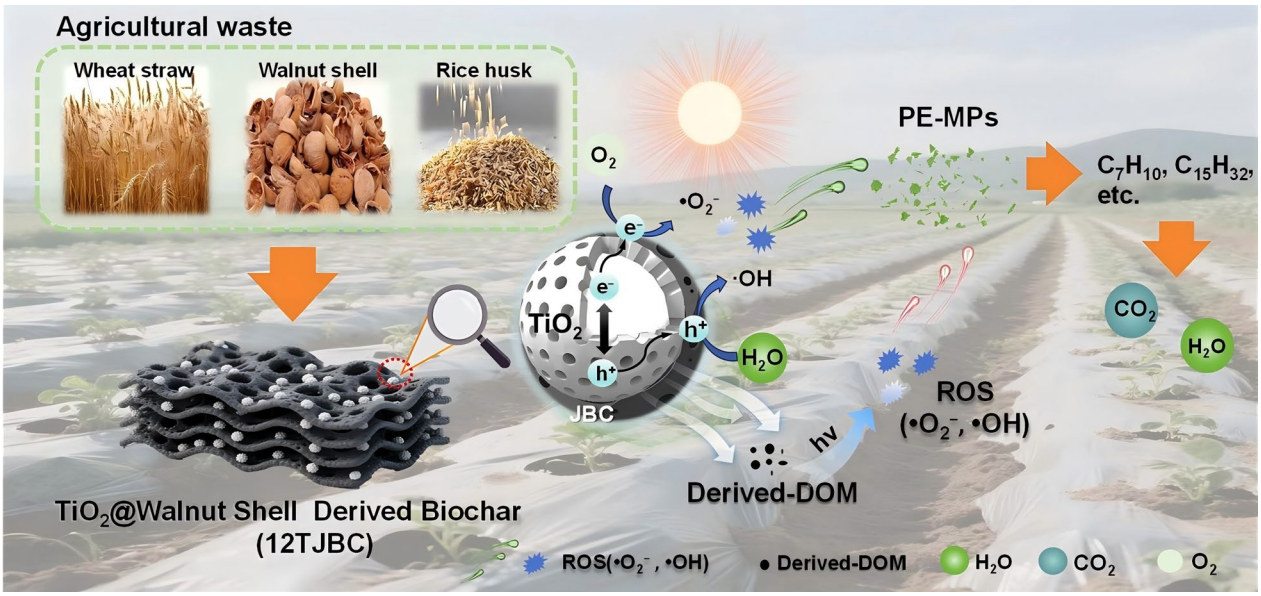

1 Introduction

Agricultural plastic mulch, predominantly polyethylene (PE)-based (50–70%), is extensively utilized nationwide for vegetable, fruit, and tuber cultivation (Cao et al. 2023). Under prolonged environmental stressors, including physical fragmentation, chemical weathering (e.g., photodegradation), and biological activity, these mulches are broken into persistent polyethylene microplastics (PE-MPs) (Qiang et al. 2023). The high bond dissociation energy of C–C and C–H bonds (330–375 kJ mol^{-1}) renders PE-MPs chemically inert and highly resistant to biodegradation, enabling them to persist in the environment for extended periods—estimated half-lives range from 200 to 400 years. Their low density further facilitates transport by hydrodynamic forces, leading to widespread distribution in surface waters and sediments. Consequently, PE-MPs frequently accumulate as pollution hotspots in urban lakes, river estuaries, and coastal zones. Notably, their concentration in sediments can be up to 100 times higher than in the overlying water (Castro et al. 2022), posing serious risks such as soil and water contamination, toxicity to organisms, and potential threats to human health (Çobanoğlu et al. 2021). Given these concerns, developing effective technologies to mitigate PE-MP pollution is urgently needed.

Recently, photocatalytic degradation has represented a promising strategy for MPs remediation due to its operational mildness and minimized secondary pollution (Zhang et al. 2023). TiO_2, as the mainstream of current photocatalysts, is widely used in the photocatalytic degradation of MPs (Ding et al. 2023). However, it suffers from rapid charge recombination and inefficient solar utilization (Ding et al. 2022). Biochar (BC) is a carbonaceous material derived from pyrolyzed agricultural waste, such as crop residues. It serves as a soil conditioner to improve water and nutrient retention, and more critically, acts as an electron-transfer mediator to facilitate photocatalysis (Chi et al. 2024; Wei et al. 2024). Integrating BC with TiO_2 creates a synergistic system where the carbon scaffold simultaneously accelerates charge separation and broadens light absorption (Li et al. 2023). Prior studies demonstrate that the graphitization degree of BC enhances interfacial charge transfer kinetics by establishing rapid electron-conduction pathways. Meanwhile, surface functional moieties, such as carbonyl groups, act as effective electron donors to suppress charge carrier recombination at the heterojunction interface (Wang et al. 2025). In addition, the wrinkled topology and hydrophobic domains of BC enable efficient polyethylene PE-MP capture via π–π interactions, thereby concentrating targets for interfacial degradation (Ho et al. 2023).

However, the interfacial properties of biochar are dictated by feedstock origin, leading to varied photocatalytic capability. For example, straw-derived biochar (K/Ca) induces TiO_2 lattice distortion that elevates oxygen vacancy concentration, while the silica matrix in rice

husk biochar could narrow the TiO_2 band gap via quantum confinement and defect engineering, extending light absorption (Zhou et al. 2024). Concurrently, dissolved organic matter (DOM) liberated from biochar during photocatalysis regulates MPs photoaging through competing light absorption and radical mediation (Yang et al. 2023). Zhang et al. used DOM derived from corn straw and pig manure biochar to investigate the effect of DOM on the photodegradation of the insecticide imidacloprid (IMI) (Zhang et al. 2020). Therefore, decoupling the BC origin and DOM-driven effects is essential to elucidate the true photocatalytic efficiency of BC/TiO_2 hybrids in MP degradation.

To overcome the inherent limitations of pristine TiO_2 and unravel feedstock-dependent BC mediation in PE-MPs degradation, three distinct biomass-derived biochar (BCs) were selected to modify core–shell structured TiO_2 (CST) via hydrothermal synthesis. The physicochemical properties of different BC@CST composites were quantitatively analyzed, correlated with their photocatalytic performance toward PE-MPs degradation. The difference in band structure modulation induced by different BC was interpreted, while EPR coupled with radical scavenging assays quantified primary reactive oxygen species. Meanwhile, the role and contribution of BC-derived DOM in the photocatalytic degradation process of PE-MPs were investigated. The molecular pathways of PE-MPs decomposition were revealed by combining two-dimensional correlation spectroscopy (2D-COS) and GC–MS, and the environmental toxicity of the intermediate products was evaluated. This strategy achieves cascade valorization of agricultural waste into functional catalysts for sustainable plastic remediation.

2 Materials and methods

2.1 Materials

The reagents used in this study were categorized into four groups. Organic solvents included glycerol ($C_3H_8O_3$, ≥99.5%, Macklin), ethanol (C_2H_5OH, AR, Macklin), diethyl ether ($C_4H_{10}O$, AR, Macklin), and tert-butyl alcohol (TBA, 99.5%, water < 0.005%, Macklin). Titanium oxysulfide ($TiSO_4$, ≥29% Ti basis, technical grade, Macklin) was employed as the metal source. For radical scavenging and quenching experiments, benzoquinone (BQ, ≥99.5%, HPLC, Macklin), ethylenediaminetetraacetic acid disodium salt (EDTA-2Na, Macklin), and 2,3-dichloro-5,6-dicyano-1,4-benzoquinone (DDQ, 98%, Macklin) were used. Reactive species capture agents included terephthalic acid (TPA, 99%, Macklin) and nitro blue tetrazolium chloride (NBT, >98%, biotechnology grade, Macklin). Wheat straw-derived biochar (WBC), rice husk-derived biochar (RBC), and walnut shell-derived biochar (JBC, 500 °C) were purchased from the straw and charcoal industry. PE-MPs (500 μm) were purchased from Hegna Plastics Company.

2.2 Catalyst preparation

The synthesis of core–shell titanium oxide (CST) followed our previous report (He et al. 2021). In brief, glycerol (12.6 g) and ethanol (20 mL) were combined in a 100-mL beaker, followed by the dropwise addition of $TiOSO_4$ (1 mL) and diethyl ether (10 mL) under stirring. After 30 min, the mixture was transferred to a stainless-steel autoclave (50 mL) and reacted in an oven at 110 °C for 48 h. The resulting precipitate was collected via centrifugation (3000 rpm, 10 min), thoroughly washed with ethanol, and dried at 60 °C for 12 h. Finally, the dried sample was calcined in a muffle furnace at 550 °C for 3 h with a rate of 5 °C min^{-1}. The obtained sample was named CST.

The biochar/CST composites were prepared using a modified CST protocol. The key difference involved incorporating varying amounts of biochar (mass ratios 1:1.2, 1:1.4, 1:1.6, and 1:1.8, labeled as 12, 14, 16, and 18, respectively) into the precursor solution. The subsequent procedures followed the standard CST preparation. The final samples were designated as xTWBC, yTRBC, and zTJBC, where x, y, and z correspond to the theoretical mass ratio of biochar (WBC, RBC, JBC) to CST in each composite in Fig. 1a.

2.3 Catalyst characterization

The crystalline structure of the CST@BC composites was characterized by X-ray diffractometers (XRD, Bruker AXS, Rigaku, Japan). The morphology of the sample was observed via a scanning electron microscope (SEM, ZEISS Sigma 360, Germany) and a high-resolution transmission electron microscope (HR-TEM, FEI Talos F200X G2, USA). Specific surface area and pore size were determined by N_2 adsorption–desorption analysis. Surface elemental composition and chemical states were probed and were analyzed using X-ray photoelectron spectroscopy (XPS, Thermo Scientific K-Alpha, USA). Raman spectroscopy (Horiba LabRAM HR Evolution, Japan) was employed to investigate chemical bonding, while surface functional groups were identified via Fourier-transform infrared spectroscopy (FT-IR, Thermo Fisher Scientific Nicolet iS20, USA). The optical absorption properties and bandgap estimation were evaluated by ultraviolet–visible diffuse reflectance spectroscopy (UV–vis–DRS). Photoluminescence spectroscopy (PL, Edinburgh FL S1000, UK) was utilized to assess photo-induced charge carrier separation efficiency. Photoelectron density (i–t curve), electrochemical impedance spectroscopy (EIS) curve, and flat-band potential analysis (Mott-Schottky curve) were performed with an electrochemical workstation

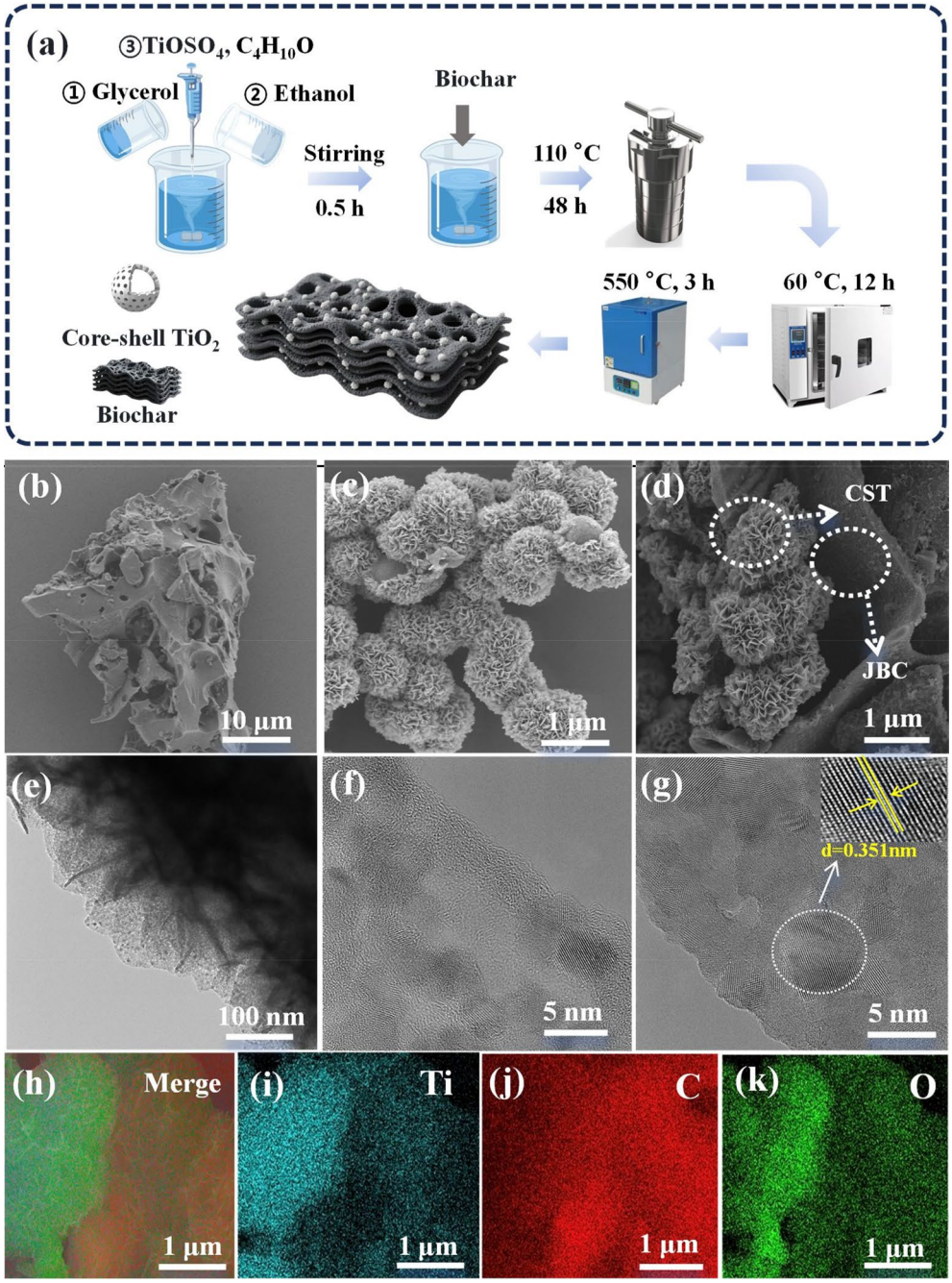

Fig. 1 **a** Schematic illustration of the hydrothermal synthesis process for core–shell TiO_2/biochar (BC/CST) composites; **b**–**d** SEM images of walnut shell biochar (JBC), TiO_2 nanoparticles (CST), and JBC/TiO_2 composite (12TJBC); **e** TEM image and **f**, **g** HR-TEM images of 12TJBC; Elemental mapping of **h** Merge, **i** Ti, **j** C and **k** O in 12TJBC

(Chenhua CHI 660E), which is provided in detail in the Supporting Information (SI, Text S1).

2.4 Photocatalytic PE-MPs degradation experiments

The photocatalytic PE-MPs degradation experiments were conducted in a photochemical reaction chamber equipped with four light bulbs (four 4 W light bulbs, F4T5/BL, λ = 300–460 nm, 1150 W cm^{-2}). Before the reaction, the prepared PE-MPs (50 mg) and catalyst (50 mg) were dispersed with ultrapure water (50 mL, 18.2 MΩ·cm) in a 100-mL quartz reactor. The slurry underwent 5-min ultrasonication under air (25% O_2/75% N_2)

purge, followed by sealing and photo-irradiation with magnetic stirring (500 rpm). After the reaction, PE-MPs were recovered with a GF/F filter (0.45 μm) for subsequent analysis. Gas products were sampled via gastight syringe (SGE μLITET™) for CO_2 quantification by GC-FID (HP-PLOT/Q column, 30 m × 0.32 mm; N_2 carrier at 2.0 mL min^{-1}; 10:1 split ratio). Wavelength-dependent effects were probed using monochromatic LED sources (365, 395, 420, 450 nm; 1150 μW cm^{-2}). Meanwhile, dark controls were also conducted for comparison. All experiments were repeated three times to reduce systematic errors.

PE-MPs after the reaction were analyzed through various methods. In brief, particle size reduction was quantified via optical microscopy (Moticam ProS5Lite) with ImageJ analysis of 200 particles per sample. Based on this analysis, particle size reduction and the mean particle size were quantified. The surface morphology alterations were examined by SEM (ZEISS Sigma 360, Germany, 5 kV) after gold sputtering. Thermal properties were determined by DSC (DSC, TAQ2000, DSC2500, USA) at 10 °C min^{-1} heating rate, with the enthalpy changes (ΔH) was analyzed. Surface oxidation was evaluated through FTIR (FT-IR, Thermo Fisher Scientific Nicolet iS20, USA) with carbonyl index calculated (Text S2), which was referred to a previous study (Syranidou et al. 2023). Additionally, hydrophilicity shifts were measured via contact angle goniometry (Chengde Dingsheng JY-82C, China). Based on the FTIR data, the changes in the surface groups of PE-MPs were explored using 2D-COS. The detailed information is provided in the SI (Text S2).

Additionally, for the DOM leached from 12TWBC, 12TRBC, and 12TJBC, dissolved organic carbon (DOC) was measured using a total organic carbon analyzer (TOC multi-N/C 3100, Jena Analytik, Germany), and absorbance at 254 nm was measured using a UV spectrophotometer (Shimadzu, UV-1900i) (Krupińska 2024). The maximum aromaticity index was calculated through comparison to investigate whether DOM exhibits a photocatalytic degradation effect on PE-MPs (Bittar et al. 2015).

2.5 ROS identification and quantitation

To identify the dominant reactive oxygen species (ROS) involved in the photocatalytic process, scavenging experiments were conducted using specific quenchers: tert-butanol (TBA) for hydroxyl radicals (•OH), benzoquinone (BQ) for superoxide anions ($•O_2^-$), disodium ethylenediaminetetraacetate (EDTA-2Na) for holes (h^+), and 2,3-dichloro-5,6-dicyano-1,4-benzoquinone (DDQ) for electrons (e^-) (Tang et al. 2021). Sufficient concentrations of each quencher were employed to ensure complete scavenging of the corresponding radicals in the reaction, with the selected dosages based on established protocols reported in prior literature (Li et al. 2022; Feng et al. 2023).

The degradation efficiency was evaluated by comparing the experimental groups with quenchers to the control group without any scavenger. The steady-state concentrations of •OH and $•O_2^-$ were quantified spectroscopically using terephthalic acid (TPA) and nitroblue tetrazolium (NBT) as molecular probes, respectively (Gao et al. 2022). To further confirm the existence of these free radicals in the photocatalytic system, electron paramagnetic resonance (EPR) spectroscopy was employed using a Bruker EMXPlus-6/1 spectrometer (Germany), as detailed in SI (Text S3).

2.6 The effect of leached DOM on PE-MPs degradation

The DOM leaching experiment was performed in a 50-mL quartz beaker. Briefly, 50 mg of each biochar-based composite (12TWBC, 12TRBC, and 12TJBC) was dispersed in 50 mL ultrapure water. Under identical photocatalytic conditions (light source: four 4 W F4T5/BL bulbs, wavelength: 300–460 nm, irradiance: 1150 μW cm^{-2}, reactor: 100-mL quartz beaker), the suspension was irradiated for 8 h. Subsequently, the leachate was filtered through a 0.22-μm MCE membrane (Hunan Beekman Holdings Co., Ltd., China) to collect DOM, designated as WDOM, RDOM, and JDOM, respectively.

The properties of DOM leached from various BC/CST composites were comprehensively characterized. The DOC of different DOM was quantified using a TOC multi-N/C 3100 analyzer (Jena Analytik, Germany). The aromaticity of the DOM was evaluated with $SUVA_{254}$ using a UV–vis spectrophotometer. Additionally, the electron transfer capabilities of the DOM samples, including electron-donating capacity (EDC) and electron-accepting capacity (EAC) (Berg et al. 2023; Yu et al. 2022), were determined via cyclic voltammetry performed on an electrochemical workstation (Chenhua CHI 660E, China). Detailed information is provided in the SI (Text S4).

To evaluate the impact of different DOM on PE-MPs degradation, the DOC content of each DOM was standardized to 10 mg L^{-1} using a TOC analyzer first. Identical photocatalytic reaction conditions (as specified in Sect. 2.4 for composite-driven degradation) were applied to DOM-treated PE-MPs systems. Post-reaction PE-MPs were collected for subsequent analysis.

Furthermore, ROS generation, including •OH and $•O_2^-$ during DOM-driven PE-MPs degradation, was quantified using identical methodologies described in Sect. 2.5. Steady-state concentrations ($[•OH]_{ss}$ and $[•O_2^-]_{ss}$) were determined via TPA and NBT probe assays (Liu et al. 2023). In addition, the light-shielding effects (S)

of different DOMs on the photodegradation of PE-MPs were also evaluated (Xue et al. 2019), with specific details presented in the SI (Text S4).

2.7 Intermediates identification and toxicity assessment

During the photocatalytic PE-MPs degradation, the solutions were separated and filtered through 0.22-μm MCE membranes (Hunan Beekman Holdings Co., Ltd.). Then it was subjected to liquid–liquid extraction using equal-volume tetrahydrofuran. The organic phase was concentrated via vacuum centrifugal evaporation (Shanghai Jingxin Industrial Development Co., Ltd.) and analyzed by gas chromatography-mass spectrometry (GC–MS, Agilent 7890, USA) to identify intermediates. Acute and chronic ecotoxicities of detected compounds toward fish (*Danio rerio*), water fleas (*Daphnia magna*), and green algae (*Raphidocelis subcapitata*) were quantitatively predicted using the ECOSAR v2.0 software based on US EPA protocols (Li et al. 2025). Meanwhile, taking mung bean as the test objects, the effects of intermediate products at different reaction times on the germination rate and growth were investigated, as detailed in Text S5 in the SI.

2.8 Statistical analysis

Statistical variations in PE-MPs particle sizes across different treatments are illustrated in Fig. 3. Data analysis was performed using SPSS 26.0 (IBM Inc.) and Microsoft Excel 2019, while figures were generated with Origin 2024 (OriginLab). Significant differences were evaluated via one-way analysis of variance (ANOVA), followed by Duncan's multiple range test for post-hoc pairwise comparisons. The significance level was set at $\alpha = 0.05$. In the figures, different lowercase letters (a, b, c, d) denote significant differences between groups ($p < 0.05$), while shared letters indicate no significant difference.

3 Results and discussion

3.1 Structural analysis of BC/CST composites

Figure 1a displays the preparation of BC/CST composite, and walnut shell biochar (JBC) displayed the morphological grooves (Fig. 1b), which could provide an effective substrate for CST combination during the hydrothermal reaction. As shown in Fig. 1c, the core–shell structure of TiO_2 was confirmed with the particle size around 1 μm. This was evidenced by the SEM images for the BC/CST composites, in which CST uniformly coated BC surfaces (Fig. 1d). TEM further corroborated CST loading onto JBC, with minimal structural alteration for CST and JBC (Fig. 1e, f). HR-TEM identified the obvious fringe spacing with 0.351 nm, assigned to anatase (101) planes (matching XRD) (Fig. 1g). Elemental mapping demonstrated homogeneous distribution of Ti, C, and O throughout the composite (Fig. 1h–k).

XRD analysis revealed that CST predominantly exhibited an anatase crystal phase (Fig. 2a), which matched well with the PDF#21–1272. The broad peak (2θ around 23°) for pristine BC signified its characteristic amorphous structure, which intensified with BC content increased in the composite. The composite displayed characteristic peaks of both CST and BC, validating well integration. During hydrothermal synthesis, the incorporation of BC may facilitate the crystallization of anatase TiO_2. N_2 adsorption–desorption isotherms revealed type IV curves with H_3/H_4 hysteresis loops across all composites (Fig. S1a), and the relevant analysis of specific surface area and pore structure is presented in Table S1. All BC/CST composite exhibited higher specific surface areas and larger pore sizes compared to the unmodified BC. This enhancement can likely be attributed to the contribution of the core–shell TiO_2 nanostructure, which not only increased the average pore diameter but also expanded the overall surface area of the composites. Notably, among the BC/CST composites, 12TJBC exhibited an enhanced specific surface area of 355.65 $m^2\ g^{-1}$ and hierarchical porosity, potentially driven by a higher density of micropores in JBC (Fig. S1b). This observation aligns with the findings of Hu et al., which confirmed that a larger specific surface area is linked to microporous structural characteristics (Hu et al. 2024).

As shown in Raman, the distinct peaks at 151 cm^{-1} and 403 cm^{-1} corresponded to the symmetric stretching and bending of Ti–O, respectively (Fig. 2b) (Taudul et al. 2023). The peak at 515 cm^{-1} was attributed to the asymmetric stretching and bending vibrations of Ti–O bonds, and the signal at 626 cm^{-1} suggested a cooperative vibration of Ti–O bonds, which are summarized in Table S2. These peaks were both found in CST and TJBC, demonstrating the presence of CST and JBC in the composite. Additionally, the peaks at 1335 cm^{-1} and 1586 cm^{-1} represented the D (indicating sp^3 carbon) and G band (indicating in-plane sp^2 carbon vibration) of JBC, respectively (Palanisamy et al. 2022). Significantly, the decrease in the I_G/I_D ratio from 0.635 in JBC to 0.435 in the TJBC suggests an elevation in carbon defects and lattice disorder, further confirming the structural modification of JBC in CST. This was further demonstrated by the FTIR. As displayed in Fig. S2 and Table S3, all BC/CST composites exhibited characteristic absorption bands at 500 cm^{-1} (Ti − O bonds), 1107 cm^{-1} (C–O–C asymmetric stretch/aromatic C–O), and 1610 cm^{-1} (C=O stretching) (Brombilla et al. 2022), implying interfacial interaction between TiO_2 and distinct BC matrices. Significantly, TJBC demonstrated maximal peak intensity at 1107 cm^{-1} relative to other BC/CST composites, revealing the

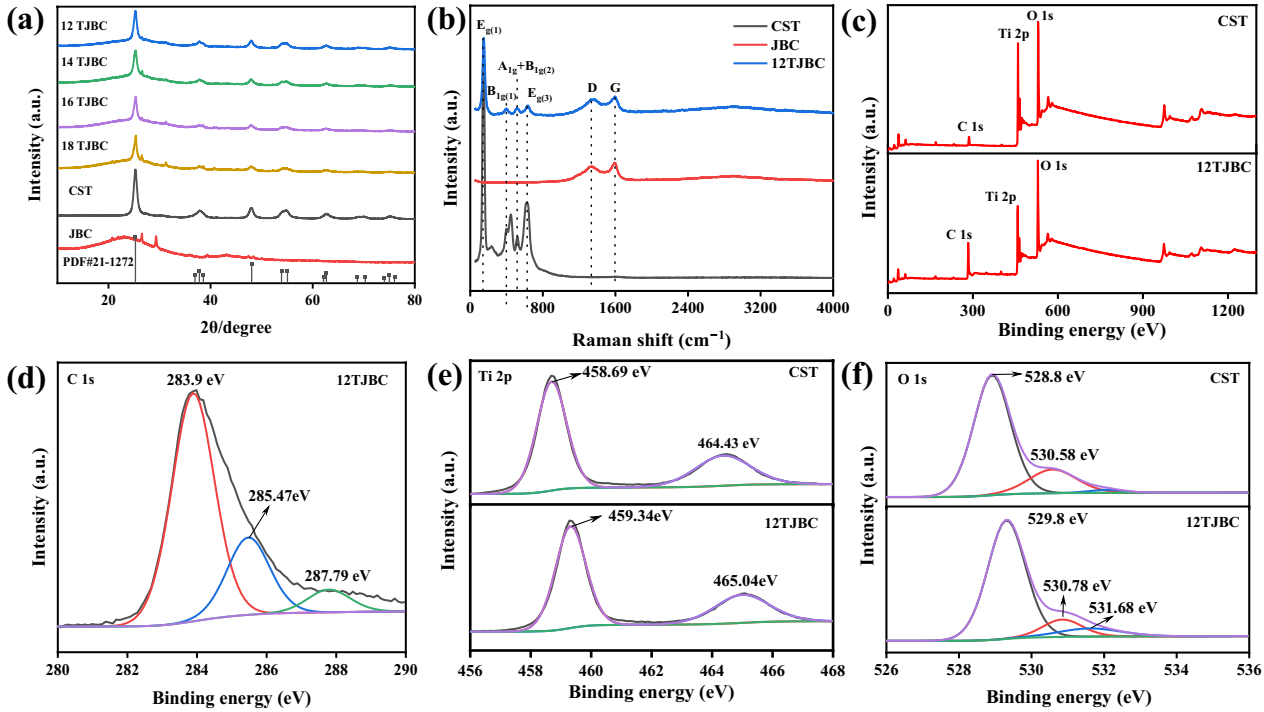

Fig. 2 **a** XRD patterns of walnut shell biochar (JBC), TiO_2 nanoparticles (CST), and TJBC composites with different biochar-to-TiO_2 ratios; **b** Raman spectra of JBC, CST, and 12TJBC; XPS analysis of **c** full spectrum, C 1 s (**d**), Ti 2p (**e**), and O 1 s (**f**) levels of CST and 12TJBC composites

intensified interfacial interactions between JBC and CST. The observed red shift of this band correlated with increased biochar loading, underscoring enhanced intermolecular forces and functional group reorganization, thereby facilitating interface formation between JBC and CST (Shi et al. 2024).

XPS analysis revealed distinct chemical states of the composites. The full spectrum of each element of CST and 12TJBC is displayed in Fig. 2c. In the C 1s spectrum (Fig. 2d), the peak at 283.9 eV corresponded to C–C bonds formed in the calcination during BC preparation. Peaks at 285.47 eV and 287.79 eV originated from O–C and O=C bonds, respectively. Characteristic peaks in the Ti 2p spectrum (Fig. 2e) of CST appeared at 458.69 eV (Ti 2p3/2) and 464.63 eV (Ti 2p1/2), respectively, exhibiting a spin–orbit splitting energy of 5.7 eV, confirming the presence of Ti^{4+}. A positive shift of these peaks in the TJBC composite indicates an electron-deficient state of Ti element. In the O 1s spectrum (Fig. 2f), the peaks at 529.8 eV and 530.78 eV were identified as the lattice oxygen and surface –OH groups on all samples, respectively (Li et al. 2019). Notably, an additional peak at 531.68 eV for TJBC suggested chemisorbed oxygen associated with oxygen vacancies (Zou et al. 2018), implying BC addition might cause more defects of TiO_2 due to the robust interfacial interaction. Significantly, the peak of lattice oxygen peak shifted negatively in the TJBC (528.88 eV) relative to CST (529.8 eV), further demonstrating electron transfer between JBC and CST. This might be due to the strong intermolecular interaction between BC and TiO_2, which facilitates electron transfer from TiO_2 to the more electronegative carbon (Santra et al. 2023).

3.2 Photocatalytic PE-MPs degradation

The PE-MPs degradation was performed in a light reaction chamber. Comparative analysis confirmed that all BC/CST composites significantly enhanced degradation kinetics relative to pure CST, primarily attributed to the BC/CST heterojunction interface facilitating efficient photogenerated electron transfer. As demonstrated in Fig. 3a, TJBC exhibited superior catalytic activity among BC variants, likely reflecting the synergistic effect of robust interfacial interactions (as verified in FTIR) and enhanced surface area providing abundant active sites for PE-MPs adsorption and reaction.

In addition, all TJBC samples with different ratios outperformed pure BC and CST (Fig. 3b), wherein 12TJBC exhibited maximal efficiency. Notably, excessive BC content may attenuate light absorption by CST. Spectral response analysis confirmed substantially accelerated degradation under illumination versus dark conditions,

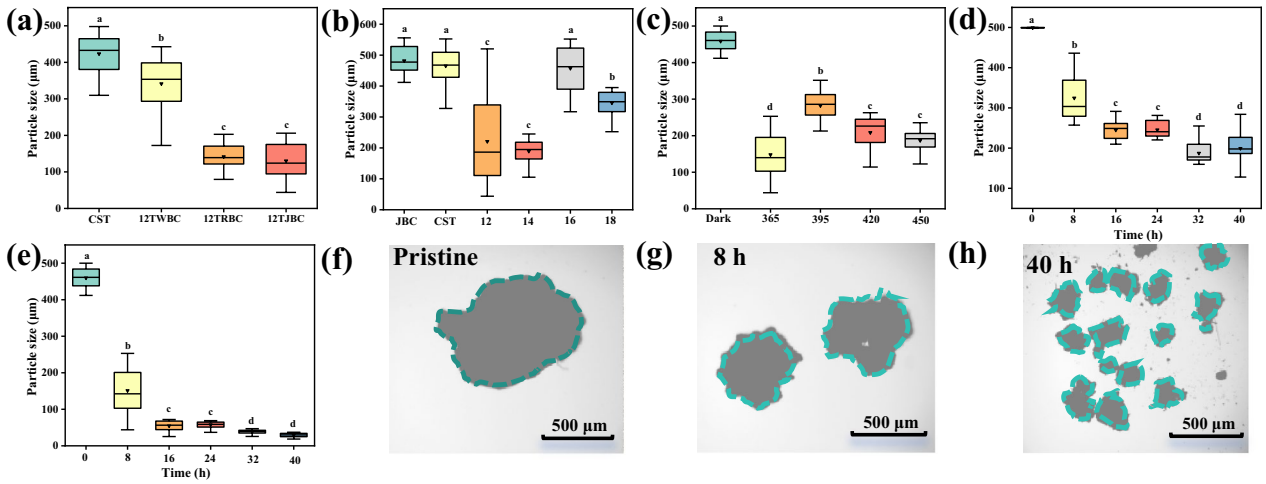

Fig. 3 Photocatalytic degradation performance of PE-MPs by CST and biochar/TiO_2 composites: **a** comparison of CST and different biochar/TiO_2 composites and **b** different biochar content in 12TJBC; **c** the effect of light wavelength on PE-MPs degradation under 12TJBC treatment; **d** time-dependent PE-MPs degradation under CST and **e** 12TJBC treatment; microscopic observations of PE-MPs at different degradation stages with **f** Pristine PE-MPs, **g** PE-MPs after 8 h irradiation, **h** PE-MPs after 40 h irradiation. Different letters (a, b, c, d) above the columns indicate statistically significant differences between groups at $p < 0.05$ according to one-way ANOVA

with UV-driven activity surpassing visible-light due to intensified light absorption by both PE-MPs and TJBC material within the UV spectrum (Fig. 3c) (Wang et al. 2024). Prolonged irradiation (40 h) reduced PE-MPs particle size from an initial 500 μm to around 200 μm in CST (Fig. 3d) and sub-70 μm fragments in 12TJBC (Fig. 3e),directly evidencing continuous photochemical fragmentation, as observed from the microscopic images of PE-MPs during the reaction (Fig. 3f–h). The particle size distribution during the recycling experiments revealed that the catalyst exhibited excellent structural stability in five consecutive cycles (Fig. S3). Also, the pH of solution was monitored and remained consistent throughout the entire reaction period, indicating a negligible effect of pH on the particle reduction of MPs (Fig. S4).

Surface morphology via SEM constitutes a critical metric for evaluating MPs degradation (Dimassi et al. 2023). It was revealed that PE-MPs developed microfibrous structures and observable surface cracking after the irradiation, though these alterations remained moderate (Fig. 4a, b). Significantly, the TJBC-treated sample exhibited exacerbated morphological deterioration (Fig. 4c), attributable to enhanced photochemical oxidation of PE-MPs (Yu et al. 2024). The alteration of surface groups of PE-MPs was further analyzed by FTIR. As delineated in Fig. 4d, a prominent carbonyl (–C=O) stretching vibration at 1728 cm^{-1} of PE-MPs after reaction was found, confirming the surface oxidation (Baysal and Saygin 2023). Moreover, this peak was more pronounced in the 12TJBC-treated samples. Additionally, the surface photo-oxidation degree of PE-MPs was quantitatively analyzed by the CI (Almond et al. 2020). It was found that the CI of PE-MPs increased after irradiation, providing definitive evidence of amplified photo-oxidation extent (Fig. 4e).

In addition to the changes in surface functional groups, we also investigated the thermal stability of PE-MPs. DSC analysis (Fig. 4f) showed that the enthalpy value of PE-MPs decreased from 100.17 J g^{-1} to 91.69 J g^{-1} after the reaction. This diminished enthalpy indicates disruption of molecular ordering within PE-MPs, likely arising from either oxygen atom incorporation during oxidation or structural defects induced by surface hydrogen abstraction (Rodríguez ChiALANZA et al. 2022).

The alteration of surface groups and structure of MPs, especially the emergence of oxidative functional groups, usually leads to changes in hydrophilicity and hydrophobicity. As shown in Fig. 4g–i, PE-MPs exhibited inherent hydrophobicity with an initial contact angle of 124.27°. After 24 h of irradiation with 12TJBC, the angle decreased to 108.02°, progressively declining to 106.74° following 40 h of irradiation. This sustained reduction demonstrates enhanced surface hydrophilicity correlated with extended photocatalytic duration (Kovinchuk et al. 2023).

2D-COS is an advanced spectroscopic analysis method developed based on traditional one-dimensional spectroscopy. As displayed in Fig. 5a–c and Table S4, the distinctive response sequence of functional groups in the synchronous spectrum (Fig. 5a–c)—particularly accelerated C–H bond perturbation in the optimized 12TJBC

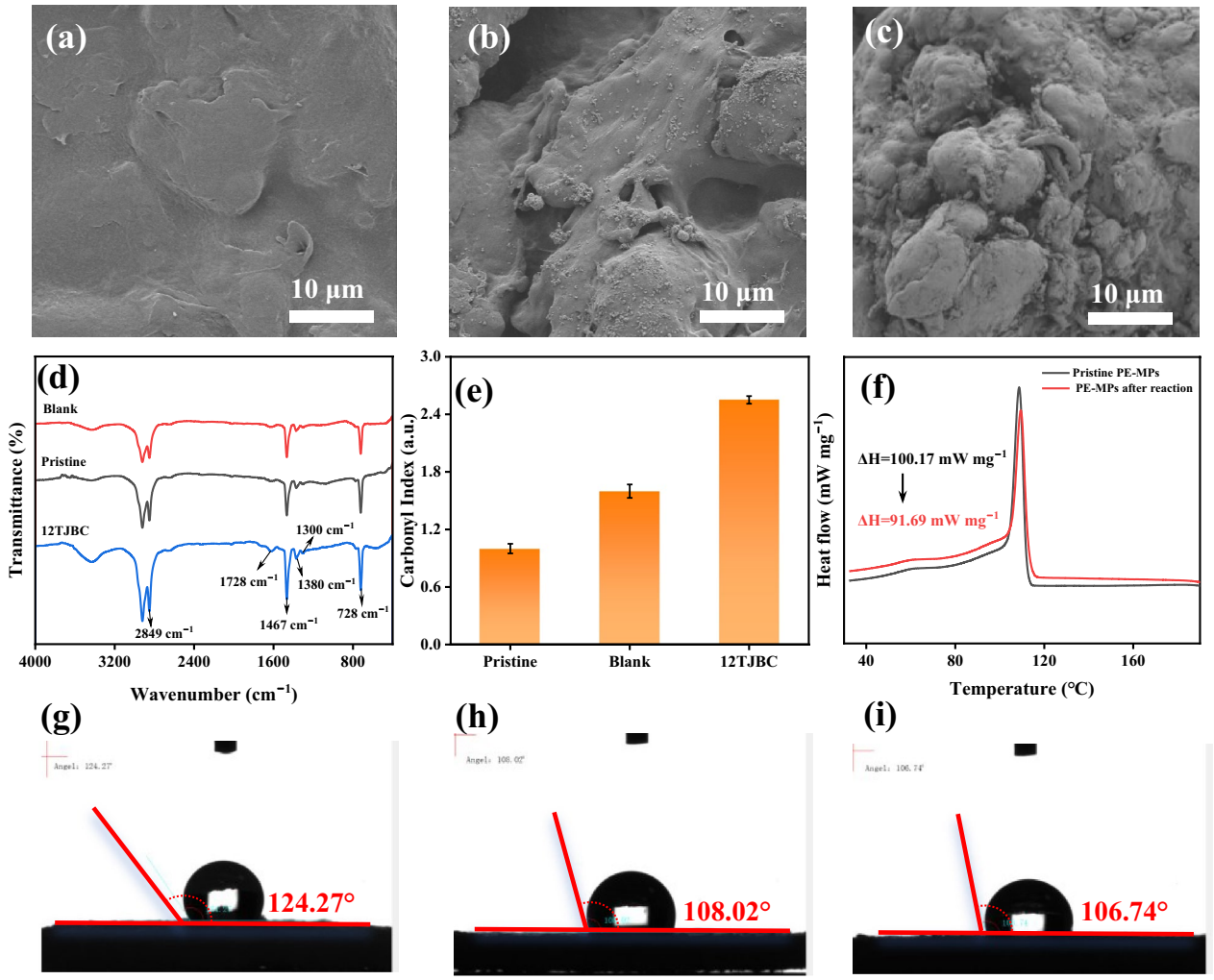

Fig. 4 SEM images of **a** pristine PE-MPs and after reaction with **b** pure photolysis and **c**12TJBC treatment; **d** FT-IR spectra of pristine PE-MPs, blank, and 12TJBC-treated samples and the corresponding **e** carbonyl index (CI) comparison; **f** DSC curves of pristine and degraded PE-MPs; Contact angles of **g** pristine PE-MPs, **h** after 24 h of irradiation and **i** 40 h of irradiation

composite compared to CST and blank—corroborated enhanced interfacial charge transfer between the biochar and TiO_2. The sequential degradation pathways of PE-MPs under all samples were also resolved (Fig. 5d–f), revealing hydrogen abstraction (C–H at 728 cm^{-1} and 2849 cm^{-1}) as the initiating step, followed by chain scission (C–C at 1300 cm^{-1}) during photodegradation. This mechanistic insight into synergistic structural decomposition of PE-MPs could advance the rational engineering of semiconductor modulation for agricultural plastic pollution mitigation.

3.3 Photochemistry activity of BC/CST composites

UV–vis–DRS demonstrated significantly enhanced visible-light absorption in all biochar-composited TiO_2 samples versus pristine CST, with bandgap narrowing confirmed through Tauc plot analysis (Fig. 6a, b). The 12TJBC sample exhibited the most pronounced redshift and broadened absorption edge compared to 12TWBC and 12TRBC, attributed to augmented photon harvesting via intrinsic microporosity and improved interfacial charge transfer dynamics. Critically, band calculations revealed a narrowed bandgap of 12TJBC (2.74 eV versus 3.19 eV of CST), indicating heightened photoexcitation efficiency under solar irradiation, leading to higher PE-MPs photocatalytic degradation. This electronic restructuring also originated from robust interfacial coupling between JBC and CST.

PL was applied to evaluate the carrier separation of the BC/CST composites (Fig. 6c). Suppressed charge recombination in all composites was evidenced by markedly reduced emission intensity at 475 nm relative to pristine CST. The minimal emission peak in the optimally formulated 12TJBC demonstrated superior electron–hole

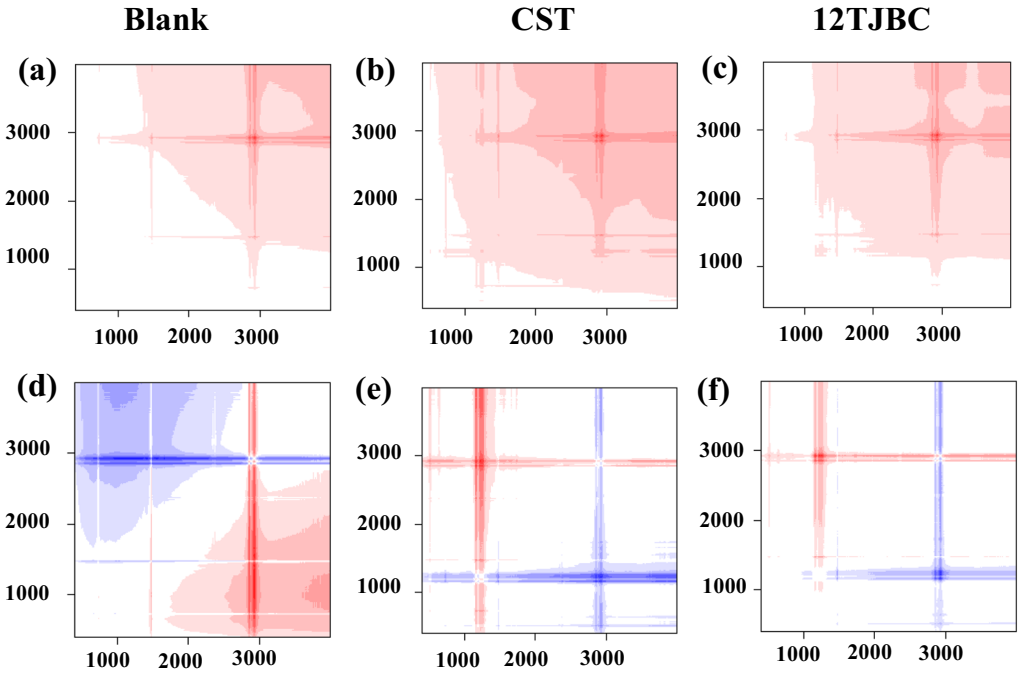

Fig. 5 2D correlation spectroscopy analysis of PE-MPs photodegradation: **a**–**c** synchronous spectrograms and **d**–**f** asynchronous spectrograms under pure photolysis (Blank), CST, and 12TJBC treatments

separation due to the JBC incorporation, facilitating prolonged carrier lifetimes crucial for advanced PE-MPs photocatalytic degradation.

To investigate the surface electron density and transfer ability of the different samples, the photocurrent and EIS were applied. As revealed in Fig. 6d, elevated photocurrent in BC/CST composites was found relative to pure CST, directly correlating with the intrinsic conductivity of BC for efficient charge extraction. Among the composites, 12TJBC exhibited maximal photocurrent due to accelerated interfacial electron transfer between JBC and TiO_2, surpassing the other BC/CST composites (TWBC, TRBC). This observation was also confirmed in the EIS. As shown in Fig. 6e, the electron transfer ability of the composite was superior to that of the pure CST, and among all BC composites, the walnut shell-derived CST exhibited optimal interfacial electron transport efficiency. Conversely, excessive BC content obstructed incident light penetration to the CST core, consequently diminishing photocurrent density and impeding electron transfer (Fig. S5a-b).

Mott-Schottky analysis confirmed the n-type semiconductor behavior of all composites through characteristic positive-slope profiles (Fig. 6f). Critically, the 12TJBC composite exhibited a cathodically shifted flatband potential (−0.75 V vs. SCE), indicating enhanced electronic conductivity from facilitated electron accumulation. Other JBC/CST composites with different ratios are displayed in Fig. S3c. This electron enrichment stems directly from tight interfacial interaction between biochar and TiO_2. Complementary UV-DRS results validated the optimized band alignment, revealing an upward-shifted valence band position that thermodynamically favors H_2O/•OH redox reactions.

3.4 ROS and BC-DOM analysis

To better explain the mechanism of photocatalytic PE-MPs degradation, ROS generation during the reaction was investigated. Quenching assays precisely delineated ROS contributions in PE-MPs degradation. Scavenging •OH induced the most severe activity suppression, confirming its dominance in the reaction, while $•O_2^-$, e^- and h^+ exhibited progressively lesser effects (Fig. 7a) with 12TJBC treatment.

Additionally, EPR result corroborated light-triggered •OH/DMPO and $•O_2^-$/DMPO adduct signals exclusively in illumination condition, with 12TJBC composites showing pronounced enhancement over CST alone—directly evidencing biochar-facilitated ROS generation (CST in Fig. 7b and 12TJBC in Fig. 7c). Crucially, oxygen vacancy (O_V) signal (g factor = 2.01) was both found in the EPR spectra of •OH and $•O_2^-$ for 12TJBC, corroborating carbon doping-induced defects observed via XPS. Notably, the intensity of the O_V signal was higher than

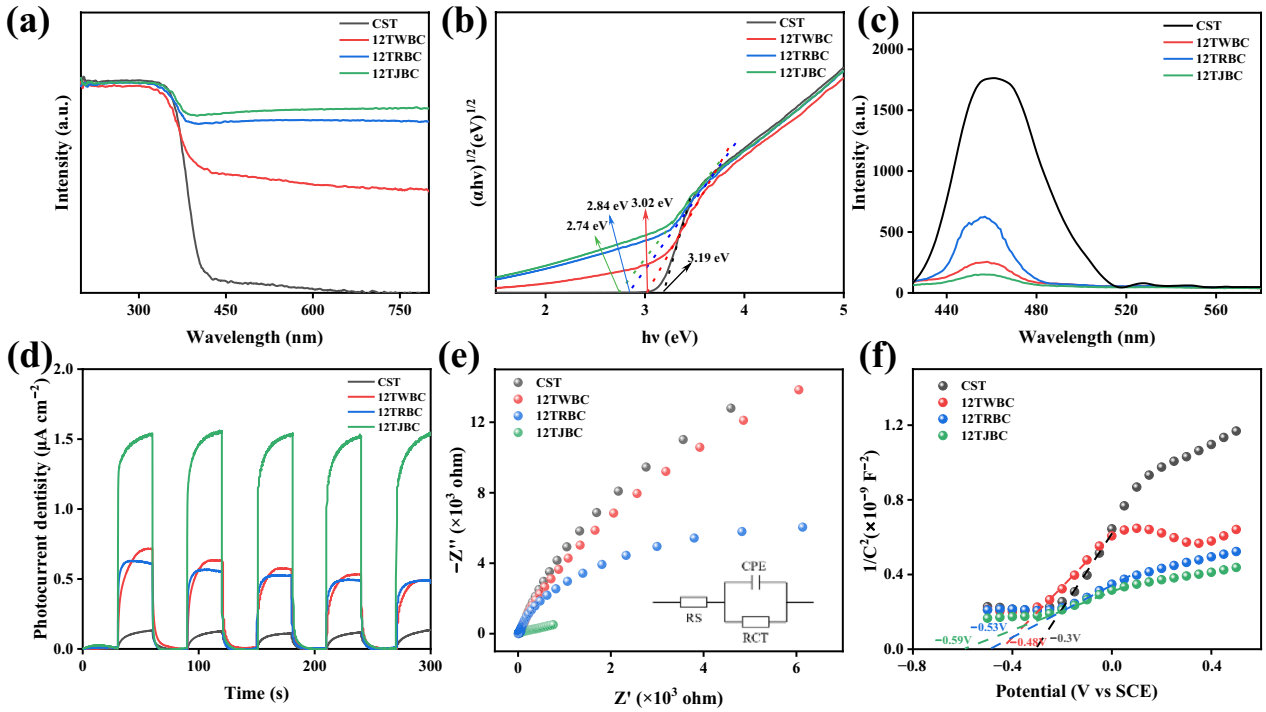

Fig. 6 **a** UV–vis DRS spectra of CST, 12TWBC, 12TRBC, 12TJBC and **b** their corresponding plots of $(\alpha hv)^{1/2}$-hv, **c** steady-state PL spectra at an excitation wavelength of 350 nm, and **d** photocurrent response under irradiation of a 300 W Xe lamp, **e** EIS curve diagram with the equivalent circuit diagram inset and **f** Mott-Schottky curves diagram of different samples

that of $\cdot O_2^-$ (Fig. S6), indicating the promoting effect of O_V on $\cdot O_2^-$ conversion to ·OH, further demonstrating the dominant role of ·OH (Wang et al. 2022). In addition, the EPR spectra of TJBC exhibited pronounced background heterogeneity, potentially originating from DOM liberated from BC during the reaction, as documented effect of MPs photochemical processes (Rangarajan et al. 2022).

Given that DOM released from BC could influence MPs photodegradation in most previous studies, the effect of DOM leachates from BC/CST composites on PE-MPs photo-degradation was explored. As displayed in Fig. 7d, it demonstrated negligible degradation under dark conditions, whereas it exhibited significant particle size reduction after 8 h of irradiation with JDOM. Meanwhile, the photochemical activity of different BC-released DOM varies due to different compositions. Comparative assessment of PE-MPs degradation of different BC-derived DOM identifies JDOM as exhibiting the most marked facilitation effect (Fig. S7a), which could be attributed to its unique molecular constituents. Consequently, a systematic investigation of dynamic DOM leaching impacts was implemented. As depicted in Fig. S7b-c, 12TJBC-leached DOM exhibited the highest DOC content compared to other BC/CST composites (12TWBC, 12TRBC), accompanied by elevated $SUVA_{254}$ values (Table S5), confirming aromatics-rich composition.

The ROS quenching experiment (Fig. 7e) revealed that the absence of ·OH in JDOM caused maximum inhibition for PE-MPs degradation (50%) relative to other radicals, implicating ·OH as the primary ROS. Meanwhile, the ratio of observed to theoretical light shielding factor for all DOMs were more than 1 (Table S5), indicating that DOM mainly plays a promoting role in the reaction, consistent with the observed performance of PE-MPs degradation by DOM. Moreover, JDOM also showed the highest electron-accepting ability (EAC) among DOM samples (Fig. 7f). These observations showed that the aromatic components in JDOM may enhance their electronic absorption capacity, thereby acquiring higher oxidation capabilities and leading to an enhancement in ·OH generation, which participates in the degradation of PE-MPs.

Therefore, it can be concluded that the dominant ROS in the reaction are ·OH, and their main sources are the TJBC and the released DOM. To quantify the contribution of the materials and their derived DOM to ROS, the steady-state concentration of ROS generated during the reaction was calculated. It revealed that TJBC exhibited synergistic ·OH amplification (8.84 μM) and

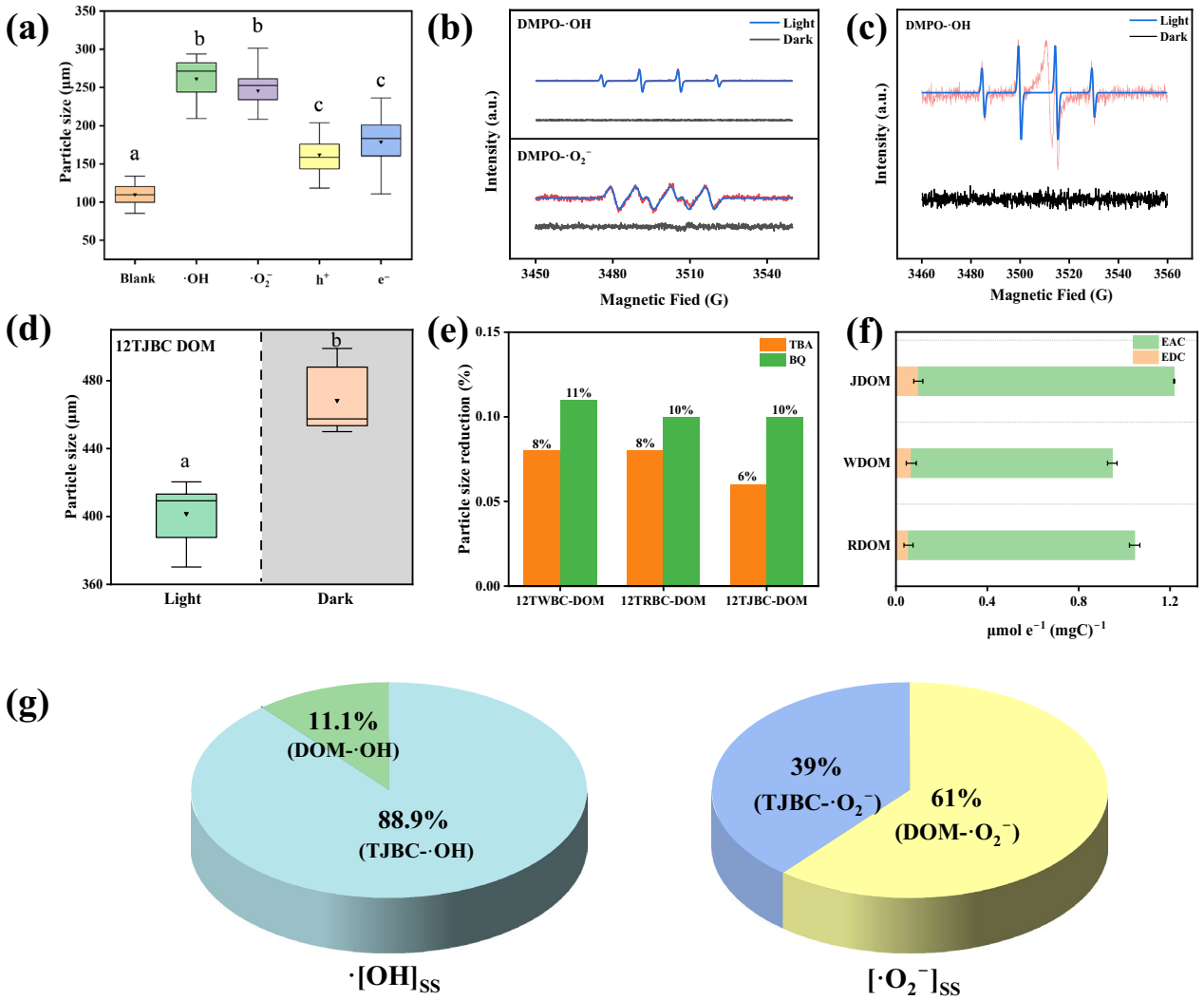

Fig. 7 **a** Quenching experiments of different reactive oxygen species (ROS); EPR signals of different radicals under dark and light conditions for **b** CST and **c** 12TJBC; particle size change of PE-MPs **d** during 12TJBC-DOM treatment; **e** after quenching the •OH and $•O_2^-$ radicals; electron transfer capacity (including electron accepting capacity (EAC) and electron donating capacity (EDC)) **f** of different BC/TiO_2 composite-deprived DOM (including 12TJBC,12TWBC,12TRBC); **g** schematic diagram illustrating the proportion of steady-state concentrations of •OH and $•O_2^-$ in 12TJBC and its deprived DOM. Different letters (a, b, c, d) above the columns indicate statistically significant differences between groups at $p < 0.05$ according to one-way ANOVA

$•O_2^-$ generation (2.21 μM), surpassing DOM-leached ROS yields (1.103 μM •OH; 1.41 μM $•O_2^-$) by 7–8 times (Fig. 7g).

3.5 Intermediate identification and environmental toxicity assessment

GC–MS was used to investigate the intermediates, and it identified key photoproducts including (1-methyl-1,2-propadienyl)-cyclopropane,2,6,10-trimethyldodecane,2-butyroctanol, 5-(1,2-propadienyloxy)−2-pentanone, and dodecane, predominantly comprising C10–C20 paraffins consistent with radical-enabled chain scission (Table S6). Oxygenated species (O–H/C=O groups) appeared sequentially as ethanol, then ketones and esters under progressive photooxidation. The concentration of CO_2 in the reaction was monitored simultaneously and showed an upward trend over time (Fig. S7d). This evolution mirrors typical free radical degradation pathways: high-molecular-weight intermediates gradually transformed into low-molecular-weight products, eventually becoming water and CO_2.

Integrating band structure analysis, ROS quantification, reaction pathway (2D-COS), and intermediates identification (GC–MS), we propose a synergistic

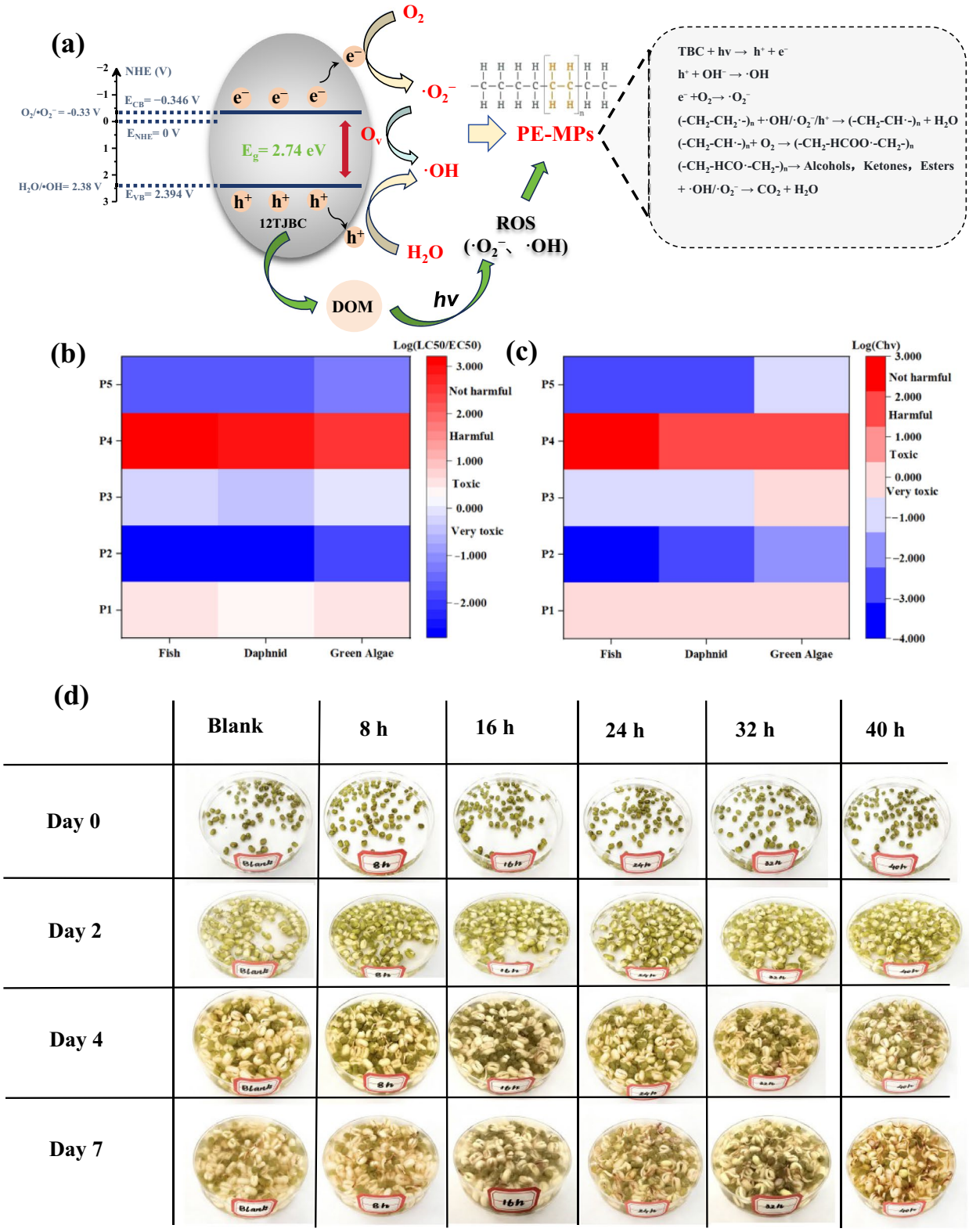

Fig. 8 **a** Band structure of 12TJBC and schematic illustration of the photocatalytic degradation pathway of PE-MPs; **b**, **c** acute and chronic toxicity assessment of intermediate products from ECOSAR; **d** germination of mung beans exposed to intermediate solutions at different reaction times

mechanism for 12TJBC-mediated PE-MPs degradation: Walnut shell-derived biochar's hierarchical porosity enhances visible-light harvesting and narrows the effective bandgap (3.19 eV → 2.74 eV), while its heterojunction interface with CST (Ti–O–C) accelerates charge separation. The efficient separation of photogenerated charge carriers could facilitate the ROS production, including •OH and $•O_2^-$. This is thermodynamically supported by the band structure of the composite, which enables water oxidation to •OH and the conversion of O_2 to $•O_2^-$ (Ur Rahman et al. 2023; Jiang et al. 2023). These ROS could initiate PE-MPs degradation via hydrogen abstraction at alkyl chains. Subsequent β-scission and ROS (•OH as dominant)-driven oxidation fragment polymer backbones into carbonyl intermediates (GC–MS-identified), with progressive oxidation culminating in terminal mineralization to CO_2/H_2O (Fig. 8a). A notable finding is that JBC enhanced the degradation of PE-MPs by generating oxygen vacancies in CST to promote the $•O_2^-$ to •OH conversion, while the DOM released from 12TJBC further contributed by mediating the production of •OH, leading to the improvement of PE-MPs degradation.

While photocatalysis presents a sustainable approach to MPs abatement, the ecotoxicological persistence of intermediate products necessitates rigorous assessment. Although the particle size reduction of PE-MPs was observed, the mineralization to CO_2 was still not optimistic. Therefore, it is necessary to assess the environmental toxicity of the intermediate products. As shown in Fig. 8b, c, the ECOSAR software was used to evaluate the acute and chronic toxicity of several intermediates to fish, water fleas, and green algae. Most intermediates were harmless, and the toxicity of alkanes was negligible compared to the harm caused by MPs themselves, demonstrating TJBC as an environmentally friendly material that can be used for the treatment of MPs in PE agricultural film. In addition, to reflect the environmental toxicity of intermediate products in real-world environments, we investigated intermediate products isolated at different reaction times and explored their impact on mung bean growth (Liu et al. 2024). As shown in Fig. 8d and Fig. S8, compared to the blank group (deionized water), the germination of mung beans in filtrates from different periods (8 h, 16 h, 24 h, 32 h, 40 h) was almost not inhibited (> 95%), and the length of the representative mung bean root selected was approximately 3 cm, indicating that the phytotoxicity of the degraded PE-MPs solution is low, and its impact on seed growth is negligible.

4 Conclusion

This study demonstrates that core–shell TiO_2 composites integrated with biomass-derived biochar (BC/CST) offer an effective strategy for the photocatalytic degradation of PE-MPs. Among them, 12TJBC, synthesized using walnut shell biochar, achieved the highest degradation efficiency due to its narrowed bandgap (2.74 eV), enhanced interfacial charge separation, and abundant ROS (•OH-dominated) generation. The porous structure and surface functionalities of JBC promoted PE-MPs adsorption and oxidation, and its leached DOM further facilitated radical-dominated degradation, whereas no notable negative light-shielding impact was found. Spectroscopic and GC–MS analyses confirmed a synergistic mechanism involving hydrogen abstraction, chain scission, and oxidative fragmentation into low-toxicity byproducts. These findings provide mechanistic insight into biomass-engineered photocatalysts and offer a sustainable route for agricultural plastic pollution mitigation.

Supplementary Information

The online version contains supplementary material available at https://doi.org/10.1007/s42773-026-00625-9.

Supplementary material 1.

Funding

This work was supported by the National Natural Science Foundation of China (52300197, 42577474).

Author contributions

Zuolong Li: Methodology, investigation, writing—original draft. Shihan Chen: Investigation, formal analysis, methodology. Yue sun: formal analysis, methodology. Yang Ding: Resources, methodology. Cheng Chen: Resources, writing—review and editing. Jiehong He: Writing—original draft, writing review and editing, funding acquisition, supervision, project administration. All authors read and approved the final manuscript.

Data availability

The datasets used or analyzed during the current study are available from the corresponding author upon reasonable request.

Declarations

Competing interests

The authors declare that they have no known competing financial interests or personal relationships that could have appeared to influence the work reported in this paper.

Author details

[1]College of Resources and Environment, Anhui Agricultural University, Anhui Provincial Key Laboratory of Hazardous Factors and Risk Control of Agri-Food Quality Safety, Hefei 230036, China. [2]College of Materials and Environmental Engineering, Hangzhou Dianzi University, Hangzhou 310018, China.

Received: 23 January 2026 Revised: 7 April 2026 Accepted: 19 April 2026
Published online: 24 June 2026

References

Almond J, Sugumaar P, Wenzel MN et al (2020) Determination of the carbonyl index of polyethylene and polypropylene using specified area under band methodology with ATR-FTIR spectroscopy. E-Polymers 20(1):369–381

Baysal A, Saygin H (2023) Multispectroscopic characterization of surface interaction between antibiotics and micro(nano)-sized plastics from surgical masks and plastic bottles. ACS Omega 8(14):12739–12751
Berg SM, Wammer KH, Remucal CK (2023) Dissolved organic matter photoreactivity is determined by its optical properties, redox activity, and molecular composition. Environ Sci Technol 57(16):6703–6711
Bittar TB, Stubbins A, Vieira AAH et al (2015) Characterization and photodegradation of dissolved organic matter (DOM) from a tropical lake and its dominant primary producer, the cyanobacteria *Microcystis aeruginosa*. Mar Chem 177:205–217
Brombilla VDL, Sarmento Lazarotto J, Silvestri S et al (2022) Biochar derived from yerba-mate (Ilex paraguariensis) as an alternative TiO_2 support for enhancement of photocatalytic activity toward Rhodamine-B degradation in water. Chem Eng Commun 209(10):1334–1347
Cao X, Liang Y, Jiang J et al (2023) Organic additives in agricultural plastics and their impacts on soil ecosystems: compared with conventional and biodegradable plastics. TrAC, Trends Anal Chem 166:117212
Castro GB, Bernegossi AC, Pinheiro FR et al (2022) The silent harm of polyethylene microplastics: invertebrates growth inhibition as a warning of the microplastic pollution in continental waters. Limnologica 93:125964
Chi W, Nan Q, Liu Y et al (2024) Stress resistance enhancing with biochar application and promotion on crop growth. Biochar 6(1):43
Çobanoğlu H, Belivermiş M, SıKDOKUR E et al (2021) Genotoxic and cytotoxic effects of polyethylene microplastics on human peripheral blood lymphocytes. Chemosphere 272:129805
Dimassi SN, Hahladakis JN, Daly Yahia MN et al (2023) Insights into the degradation mechanism of PET and PP under marine conditions using FTIR. J Hazard Mater 447:130796
Ding P, Ji H, Li P et al (2022) Visible-light degradation of antibiotics catalyzed by titania/zirconia/graphitic carbon nitride ternary nanocomposites: a combined experimental and theoretical study. Appl Catal B 300:120633
Ding C, Lu Y, Xiang M et al (2023) Internal electric field-assisted copper ions chelated polydopamine/titanium dioxide nano-thin film heterojunctions activate peroxymonosulfate under visible light to catalyze degradation of gatifloxacin: theoretical calculations and biotoxicity analysis. J Colloid Interface Sci 646:275–289
Feng H, Liu M, Tang T et al (2023) Insights into the efficient ozonation process focusing on 2,4-di-tert-butylphenol – A notable micropollutant of typical bamboo papermaking wastewater: Performance and mechanism. J Hazard Mater 443:130346
Gao J, Nunes RF, O'shea K et al (2022) UV/Sodium percarbonate for bisphenol A treatment in water: impact of water quality parameters on the formation of reactive radicals. Water Res 219:118457
He J, Lyu P, Li D et al (2021) Bio-alcohol induced self-assembly of heterojunctioned TiO_2/WO_3 composites into a hierarchical yolk-shell structure for photocatalysis. Chem Commun 57(56):6883–6886
Ho T-BC, Nguyen TB, Chen CW et al (2023) Influence of aging processes on PE microplastics with various oxidants: Morphology, chemical structure, and adsorption behavior toward tetracycline. Environ Technol Innovat 31:103173
Hu L, Wu W, Hu M et al (2024) Double-walled Al-based MOF with large microporous specific surface area for trace benzene adsorption. Nat Commun 15(1):3204
Jiang Y, Li S, Fan X et al (2023) Recent advances on aerobic photocatalytic methane conversion under mild conditions. Nano Res 16(11):12558–12571
Kovinchuk I, Haiuk N, Lazzara G et al (2023) Enhanced photocatalytic degradation of PE film by anatase/γ-MnO_2. Polym Degrad Stab 210:110295
Krupińska I (2024) Application of Fenton's reaction for removal of organic matter from groundwater. Molecules 29(21):5150
Li G, Huang J, Chen J et al (2019) Highly active photocatalyst of Cu_2O/TiO_2 octahedron for hydrogen generation. ACS Omega 4(2):3392–3397
Li L, Han Q, Wang L et al (2022) Dual roles of MoS_2 nanosheets in advanced oxidation processes: activating permonosulfate and quenching radicals. Chem Eng J 440:135866
Li D, Fang Y, Lu J et al (2023) Enhanced biodegradation of PAHs by biochar and a TiO_2@biochar composite under light irradiation: photocatalytic mechanism, toxicity evaluation and ecological response. Chem Eng J 458:141495
Li Q, Fu F, Yan J et al (2025) Synthesis of N-doped porous biochar from chemical pollutant for efficient sulfadiazine degradation: performance, mechanism and bio-toxicity assessment. Sep Purif Technol 353:128432
Liu W, Lu Y, Dong Y et al (2023) A critical review on reliability of quenching experiment in advanced oxidation processes. Chem Eng J 466:143161
Liu G-C, Yi X-H, Chu H-Y et al (2024) Floating MIL-88A(Fe)@expanded perlites catalyst for continuous photo-Fenton degradation toward tetracyclines under artificial light and real solar light. J Hazard Mater 472:134420
Palanisamy M, Perumal R, Pol VG (2022) Mesoporous weaved turbostratic nanodomains enable stable Na^+ ion storage and micropore filling is revealed to be more unsafe than adsorption and deintercalation. ACS Appl Mater Interfaces 14(1):684–697
Qiang L, Hu H, Li G et al (2023) Plastic mulching, and occurrence, incorporation, degradation, and impacts of polyethylene microplastics in agroecosystems. Ecotoxicol Environ Saf 263:115274
Rangarajan G, Jayaseelan A, Farnood R (2022) Photocatalytic reactive oxygen species generation and their mechanisms of action in pollutant removal with biochar supported photocatalysts: a review. J Clean Prod 346:131155
Rodríguez CHIALANZA M, Favre Samarra S, PéREZ PARADA A (2022) Modeling microplastic with polyethylene (PE) spherical particles: a differential scanning calorimetry approach for quantification. Environ Sci Pollut Res 29(2):2311–2324
Santra B, Pal S, Saha S et al (2023) Tailoring structural, chemical, and photocatalytic properties of ZnO@β-SiC composites: the effect of annealing temperature and environment. ACS Omega 8(26):24113–24124
Shi C, An Y, Gao G et al (2024) Insights into selective glucose photoreforming for coproduction of hydrogen and organic acid over biochar-based heterojunction photocatalyst cadmium sulfide/titania/biochar. ACS Sustain Chem Eng 12(7):2538–2549
Syranidou E, Karkanorachaki K, Barouta D et al (2023) Relationship between the carbonyl index (CI) and fragmentation of polyolefin plastics during aging. Environ Sci Technol 57(21):8130–8138
Tang Y, Kang J, Wang M et al (2021) Catalytic degradation of oxytetracycline via $FeVO_4$ nanorods activating PMS and the insights into the performance and mechanism. J Environ Chem Eng 9(5):105864
Taudul B, Tielens F, Calatayud M (2023) On the origin of Raman activity in anatase TiO_2 (nano)materials: an ab initio investigation of surface and size effects. Nanomaterials 13(12):1856
Ur Rahman Z, Shah U, Alam A et al (2023) Photocatalytic degradation of cefixime using CuO-NiO nanocomposite photocatalyst. Inorg Chem Commun 148:110312
Wang S, Zhu J, Li T et al (2022) Oxygen vacancy-mediated CuCoFe/Tartrate-LDH catalyst directly activates oxygen to produce superoxide radicals: transformation of active species and implication for nitrobenzene degradation. Environ Sci Technol 56(12):7924–7934
Wang Q, Chen M, Min Y et al (2024) Aging of polystyrene microplastics by UV/sodium percarbonate oxidation: organic release, mechanism, and disinfection by-product formation. J Hazard Mater 464:132934
Wang Y, Wang H, She T et al (2025) Transition metal induced interfacial d-p orbital hybridization boosting biochar for efficient fenton-like decontamination. Sep Purif Technol 359:130859
Wei X, Zhang X, Jin L et al (2024) Waste biomass-derived biochar in adsorption-photocatalytic conversion of CO_2 for sustainable energy and environment: evaluation, mechanism, and life cycle assessment. Appl Catal B: Environ Energy 351:123957
Xue S, Sun J, Liu Y et al (2019) Effect of dissolved organic matter fractions on photodegradation of phenanthrene in ice. J Hazard Mater 361:30–36
Yang F, Xue Y, Gao Y et al (2023) Biochar-derived dissolved organic matters influencing bacterium characteristics during biodegradation of sulfamethoxazole and chloramphenicol under alternation of visible and avoiding light. Biochar 5(1):9
Yu W, Chu C, Chen B (2022) Enhanced microbial ferrihydrite reduction by pyrogenic carbon: impact of graphitic structures. Environ Sci Technol 56(1):239–250
Yu F, Qin Q, Zhang X et al (2024) Characteristics and adsorption behavior of typical microplastics in long-term accelerated weathering simulation. Environ Sci Process Impacts 26(5):882–890
Zhang P, Shao Y, Xu X et al (2020) Phototransformation of biochar-derived dissolved organic matter and the effects on photodegradation of imidacloprid in aqueous solution under ultraviolet light. Sci Total Environ 724:137913

Zhang Z, Liang J, Zhang W et al (2023) Modified-pollen confined hybrid system: a promising union for visible-light-driven photocatalytic antibiotic degradation. Appl Catal B 330:122621
Zhou Y, Sun M, Lin C (2024) Study on the preparation of CdS/TiO_2 corn straw biochar composite materials for photocatalytic reduction of CO_2 and collaborative H_2 production. Environ Sci Pollut Res Int 31(35):48222–48232
Zou Y, Yang K, Chen Q et al (2018) Molten salt construction of stable oxygen vacancies on TiO_2 for enhancement of visible light photocatalytic activity. RSC Adv 8(64):36819–36825